# Grid Sensitivity Studies for Single and Multi-Step Ice Accretion using Unstructured Meshes

AVANI GUPTA[1], LAKSHMI N. SANKAR[2]
[1]Turbomachinery Manufacturing and Design,
Linde Inc.,
175 East Park Dr., Tonawanda, NY 14150,
UNITED STATES OF AMERICA

[2]Daniel Guggenheim School of Aerospace Engineering,
Georgia Institute of Technology,
270 Ferst Dr., Atlanta, GA 30313,
UNITED STATES OF AMERICA

*Abstract:* - The effects of grid spacing and time step sizes have been studied on an unstructured grid for a NACA 0012 glaze ice case. The methodology involving the mesh generation, the flow field computation, the collection efficiency of the water droplets, and ice accretion is discussed, and the formulation is documented. The surface grid density and boundary layer resolution effects on the predicted ice shape are considered. Relevant parameters such as the surface pressure, skin friction distribution, droplet collection efficiency, and ice shape predictions are presented and compared for the various grids. The impact of the surface $y^+$ is also discussed. Based on the comparison of the predicted ice shapes against measured shapes and the computational costs associated, recommendations for a suitable mesh size and surface resolution are made.

*Key-Words:* - Ice Accretion, Extended-Messinger Model, Grid and Time-Step Sensitivity, Dispersed Phase, Droplet Impingement, Glaze Icing, Boundary-Layer Refinement, Skin Friction Coefficient, Pressure Coefficient, Collection Efficiency.

Received: June 25, 2024. Revised: December 16, 2024. Accepted: December 28, 2024. Published: December 31, 2024.

## 1 Introduction

While advancements in flight technology have made flying safer, the requirement to operate in different weather conditions has also manifested itself strongly. This includes weather conditions that are conducive to the formation of ice. Ice can severely degrade performance resulting in a reduction or loss of lift, early stall, and increased drag. This impacts both the range of operability and the cost of operation of the air vehicles. Ice accretion does not just adversely affect the aerodynamics but also the stability and trim of a vehicle. This happens when ice accretion takes place on horizontal and vertical stabilizers. In other cases, it impacts the operational envelope including service ceiling, maximum gross weight, maximum forward speed, and endurance as a result of an increased power consumption as in the case of ice formation on propellers and rotors. When ice accreted on rotors is shed due to the centrifugal forces, this poses a severe safety hazard because this shed ice can hit other essential components of the vehicle in flight and cause failure. Thus, it is essential that the ice accretion be effectively modeled, and its impact on performance and operability be accurately predicted.

Various studies have been conducted in the past to effectively model ice accretion and determine the various parameters that influence this analysis. The AIAA Ice Prediction Workshops [1], [2] summarize the state of the art and the capabilities of the current methodologies and solvers. ONERA's IGLOO [3], [4] has options for both two and three-dimensional ice accretion simulations. ICEPAC [5] developed at the Seoul National University utilizes unstructured tetrahedral meshes for ice accretion studies. Politecnido di Milano's PoliMIce [6], [7] toolkit invokes mesh deformation to model the accreted ice. CIRA [8], [9] uses an OpenFOAM-based framework for the calculations of the flow properties and the transport of the water droplets. Studies using the FENSAP-ICE [10], [11] utility within ANSYS have also been documented. The Austrian Institute of Technology [12] and Kingston University [13] have also conducted studies using the toolkits available within ANSYS. The National

Research Council of Canada [14] applies a morphogenetic approach for surface roughness modeling for ice accretion. Polytechnique Montreal's CHAMPS [15] also explores this option. Algorithms to optimize the surface mesh quality have also been explored, [16]. Current ice accretion methodologies have been extended to study ice accretion on UAVs, [17].

For this study, an ice accretion methodology involving multiple steps, using a combination of commercial and in-house tools is developed and tested. The grids employed for each step in this process can have a significant impact on the accuracy of the ice shape prediction. The two factors at play that may impact the predicted shape of the ice accreted are the numerical drivers and the actual flow physics. In an attempt to negate the numerical impact, grid sensitivity studies using unstructured grids are carried out.

The process involves four separate steps. Pointwise is first used to generate the unstructured grids. Next, the single-phase flow field is solved using ANSYS Fluent, followed by the computation of the droplet phase. An in-house tool developed for the computation of the droplet phase and the impingement collection efficiency called GTDROP-Uns [18] is employed. For the last step, the accreted ice shape is computed on an input surface geometry by the in-house tool GT-ICE, [19]. The methodology is discussed in more detail in the subsequent chapter.

# 2 Problem Formulation

## 2.1 Methodology

The first step of the ice accretion simulation process is the mesh generation. A clean surface geometry is used for this. Next, the single-phase air flow field around this clean configuration is solved. Several essential flow field parameters are obtained from this step, including the surface temperature and the coefficients of pressure and skin friction along the surface. Following this the results from the single-phase continuum computation are provided as input for the droplet-phase computation. The dispersed phase solver solves for the velocity flow-field of water droplets which is used to compute the collection efficiency of the impinging droplets onto the airframe surface. For the final step, the information from both the air phase flow-field computation and the water droplet computation is provided as input to the icing solver. This tool computes the thickness of the accreted ice at every surface grid point and projects this orthogonally to obtain an accreted ice shape. This ice shape serves as the "equivalent" geometry for the airframe for the next time step.

The entire process is repeated for a multi-time step approach. The air and droplet flow fields around an iced airframe are recomputed, and an updated iced airframe shape is obtained. This process is carried out such that any changes in the crucial parameters like the surface pressure and skin friction distribution, the surface temperature, and the droplet collection efficiency are accounted for accurately. It must be noted that although the multi-step approach improves the accuracy of the prediction, it also adds considerable computational costs. Figure 1 shows details of the various steps in the present approach, [18].

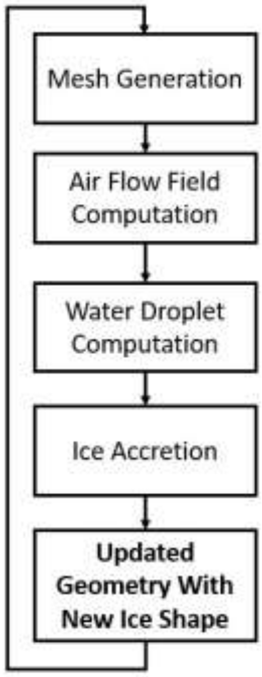


Fig. 1: Illustration for the multi-step ice accretion methodology followed in this work

### 2.1.1 ANSYS Fluent

As has been mentioned in the introduction, ANSYS Fluent is used to compute the air flow field. Since the airframe geometry is unchanging for this step, a steady-state simulation is carried out. To accurately compute the surface temperature, the solution of the internal energy is also carried out. The compressible form of the Navier-Stokes equations is solved, accounting for compressibility effects. Although, this is not a concern for the freestream Mach number for the cases chosen for this study, the capability to handle cases where compressibility is a factor exists. The energy equation is coupled to the continuity and momentum equations and solved in a coupled manner to capture the effects of compressibility. The density-based solver within Fluent is used, [20]. The effect of turbulent mixing within the mean flow is modeled using the k-omega SST turbulence model selected. For most RANS based simulations, to model turbulence either a one-equation or a two-equation model is chosen. Amongst the two-equation eddy viscosity turbulence models available, the k-omega SST is a widely accepted, industry-standard model. It behaves like the Wilcox k-omega model in regions near the wall and as the k-epsilon model in regions away from the wall, effectively blending the two models. The ideal gas equation is used for the computation of density and the viscosity is modeled as a function of temperature using Sutherland's law, [21].

The temporal discretization is implicit. Roe-FDS is used to compute the flux. The spatial discretization, both the turbulent kinetic energy and the specific dissipation, is second-order upwind. The Courant number used is 0.5. Ambient flow conditions are used to initialize the computation.

For the far-field boundaries of the grids generated, the "Inlet Velocity" boundary condition is specified. The components of the freestream velocity are calculated using the experimental angle of attack of the airfoil tested. The inlet temperature is set to the ambient temperature specified in the experimental data. At the outlet, the pressure is set to atmospheric pressure. The airfoil surface is specified to be a "No Slip" and "Adiabatic" wall with no heat transfer. The heat transfer is calculated later within the ice accretion module using the coefficient of skin friction derived from the flow field simulation. The "Standard" roughness model within ANSYS Fluent is utilized.

### 2.1.2 GTDROP-Uns

GTDROP-Uns [18] is an in-house unstructured grid-based Eulerian droplet transport tracking solver. Tetrahedral volume cells and triangular surface cells can be accommodated. The mesh and the converged air flow field are imported as FAST format grid and solution files. The same boundary conditions as specified in the previous section are used, except for the airfoil wall boundary. It is discussed later in this section. The equations for the conservation of mass and momentum are solved. These are represented in their non-dimensional form in Eqs. 1 and 2. The source terms for the conservation of momentum include the drag force between the water droplets and the airflow, the gravitational force, and the buoyant force.

$$\frac{\partial}{\partial t}\iiint \alpha_w dV + \oiint \alpha_w \boldsymbol{V_w}.d\boldsymbol{A} = 0 \tag{1}$$

$$\frac{\partial}{\partial t}\iiint \alpha_w \boldsymbol{V_w} dV + \oiint (\alpha_w \boldsymbol{V_w})\boldsymbol{V_w}.d\boldsymbol{A} = \frac{\boldsymbol{F_{wa}^{drag}} + \boldsymbol{F^{gravity}} - \boldsymbol{F^{buoyant}}}{\rho_w} \tag{2}$$

Here, $\alpha_w$ is the water volume fraction, $\mathbf{V_w}$ is the water velocity, A is the area of the cell face, V is the cell volume, and t is time. $F^{drag}$, $F^{gravity}$ and $F^{buoyant}$ are the drag, gravitational, and buoyant force terms as shown under Eqs. 3 to 5.

$$\frac{\boldsymbol{F_{wa}^{drag}}}{\rho_w} = \frac{\boldsymbol{V_s}}{V_{inf}}\frac{C_D Re_d \alpha_w dV}{24K} \tag{3}$$

$$\frac{\boldsymbol{F^{gravity}}}{\rho_w} = \frac{\alpha_w dV}{Fr^2}\frac{\boldsymbol{g}}{g} \tag{4}$$

$$\frac{\boldsymbol{F^{buoyant}}}{\rho_w} = \frac{\rho_{air}}{\rho_w}\frac{\alpha_w dV}{Fr^2}\frac{\boldsymbol{g}}{g} \tag{5}$$

K is the inertia parameter, as shown in Eq. 6. Fr is the Froude number, as shown in Eq. 7. **g** is the vector associated with the acceleration due to gravity. $V_{inf}$ is the freestream velocity magnitude.

$$K = \frac{\rho_w D^2 V_{inf}}{18L\mu_{air}} \tag{6}$$

$$Fr = \frac{V_{inf}}{\sqrt{Lg}} \tag{7}$$

D is the droplet diameter, L is a reference length which in this case is the chord length of the airfoil, and $\mu_{air}$ is the dynamic viscosity of air. The Stokes' method is used to calculate the drag between the water droplets and the airflow. The Droplet Reynolds number ($Re_d$), as shown in Eq. 8 is based on the droplet diameter and the slip velocity, which is the difference in the air and water velocities, and is used to compute the coefficient of drag as shown in Eq. 9.

$$Re_d = \frac{\rho_{air} D|\boldsymbol{V_{air}} - \boldsymbol{V_w}| * V_{inf}}{\mu} \tag{8}$$

$$C_D = \begin{cases} \frac{24}{Re_d}\left(1 + 0.15 Re_d^{0.678}\right) & Re_d \leq 1000 \\ 0.4 & Re_d > 1000 \end{cases} \tag{9}$$

The second-order Runge-Kutta numerical scheme, explicit in time, is used. Local time stepping is used to reduce computational cost. A first-order upwind scheme is employed for spatial marching. Velocities at the cell face centers are computed using inverse distance weighting.

The surface normal water velocity with the respective water volume fraction is used to compute a non-dimensional parameter called the collection efficiency. This is the impinging mass flow rate of water normalized by the freestream LWC (liquid water content) and the freestream velocity and its values vary between 0 and 1, with 0 indicating no impingement, and 1 indicating maximum possible impingement for the given set of ambient conditions.

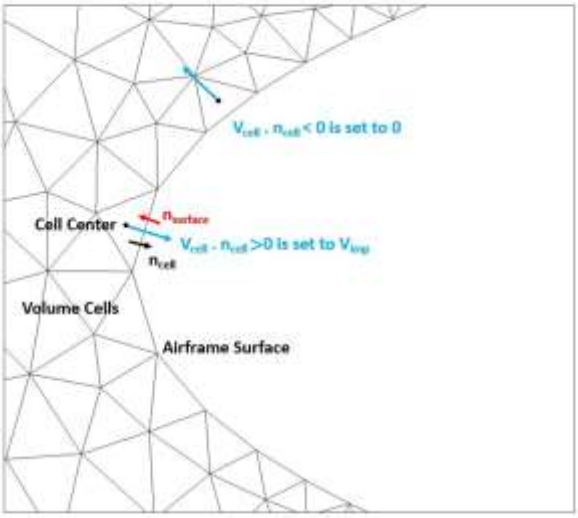


Fig. 2: Illustration explaining impingement for GTDROP-Uns' porous wall boundary condition

The wall boundary for the droplet-phase solver is set to a porous condition, [18], [22]. Mathematically, if the dot product between the droplet velocity at the cell center adjacent to the wall boundary and the normal vector at the wall boundary is positive, it indicates water leaving the wall, which is not physical. In this case, the impingement velocity is set to zero. If the dot product is negative, it indicates water entering the wall boundary, in which case the magnitude of the dot product is set to the impingement velocity. This is illustrated in Fig. 2.

### 2.1.3 GT-ICE

The heat transfer coefficient is calculated using the Reynolds Analogy. Thwaites method [23] is used for the laminar region and the method of Kays and Crawford [24] is used for the turbulent region. The transition from laminar to turbulent is determined based on the Von Doenhoff Criterion [25] which is based on the Roughness of Reynolds Number.

GT-ICE [19] is based on the Extended-Messinger [26] approach which solves a total of four equations. Two equations are used to model the temperature gradients in the ice and water layers respectively as shown under Eqs. 10 and 11. T is the temperature within the ice layer, θ is the temperature within the water layer, z is the coordinate normal to the surface, $C_{p,i}$ and $C_{p,w}$ are the specific heats at constant pressure for ice and water respectively, $k_i$ and $k_w$ are the thermal conductivities of ice and water respectively.

The conservation of mass is shown under Eq. 12. The two terms on the left land side represent the mass in the ice and water layers and the three terms on the right-hand side represent the impingement, the runback, and mass lost due to evaporation or sublimation respectively. B is the thickness of the ice layer, h is the thickness of the water layer, LWC is the freestream Liquid Water Content, and β is the collection efficiency.

The phase change equation at the interface between the ice and water layers (Stefan condition [27]) is shown under Eq. 13. $L_F$ is the latent heat of fusion [22].

$$\frac{\partial T}{\partial t} = \frac{k_i}{\rho_i C_{pi}} \frac{\partial^2 T}{\partial z^2} \tag{10}$$

$$\frac{\partial \theta}{\partial t} = \frac{k_w}{\rho_w C_{pw}} \frac{\partial^2 \theta}{\partial z^2} \tag{11}$$

$$\rho_i \frac{\partial B}{\partial t} + \rho_w \frac{\partial h}{\partial t} = (LWC)\beta V_\infty + \dot{m}_{in} - \dot{m}_{e,s} \tag{12}$$

$$\rho_i L_F \frac{\partial B}{\partial t} = k_i \frac{\partial T}{\partial z} - k_w \frac{\partial \theta}{\partial z} \tag{13}$$

A spatial marching process is adopted where any leftover water that does not freeze in a volume cell is carried over to the next cell as runback. Only two different ice density values are specified based on whether the type of ice accreted is rime or glaze. The density values used are 880 kg/m$^3$ for rime ice and 917 kg/m$^3$ for glaze ice. The ice thickness at every surface point is provided as output. This is then projected orthogonal to the surface to obtain the coordinates for the iced shape.

## 2.2 Case Studied

For the purposes of this study, a two-dimensional NACA0012 airfoil case is chosen. This is owing to the restrictions on the availability of experimental data and the significant computational costs associated with running three-dimensional simulations.

For ice accretion, when the ambient temperature is very low, most of the impinged droplets freeze immediately upon contact. This case is known as rime ice. However, when the ambient temperature is higher and closer to freezing, the water droplets impinging onto the surface do not freeze immediately. Rather a layer of water is created which may flow back and freeze at different locations on the airfoil instead of just at the leading edge. These conditions also lead to the formation of ice horns and fall under the case of glaze ice. The conditions considered in this study are listed in Table 1 and are derived from associated experimental studies, [28].

Table 1. Ambient conditions for NACA0012 glaze ice case studied, [28]

| Property | Value |
|---|---|
| **Static Temperature (K)** | 262.04 |
| **Freestream Velocity (m/s)** | 102.8 |
| **LWC (g/m$^3$)** | 1.0 |
| **MVD (µm)** | 20 |
| **Chord Length (m)** | 0.53 |
| **Total Spray Time (s)** | 231 |
| **Angle of Attack (°)** | 3.5 |

## 3 Problem Solution

A three-dimensional grid with symmetric boundary conditions along the span is used to simulate an infinite wing to obtain the air and droplet flow fields. The relevant parameters are extracted along a two-dimensional slice for input to GT-ICE.

Multi-step and single-step ice accretion simulations are carried out for each mesh studied to determine the impact of the updated flow field on the accreted ice shape and the influence of the frequency of the updates.

The surface point density plays a crucial role in determining the accuracy of the ice shape prediction. A smaller density of surface grid points leads to the loss of precision due to the larger spaces between consecutive points. Gradients in the flow properties are not captured effectively, specifically for regions around the ice horns. Conversely, a larger grid density massively impacts the computational cost associated with the air and droplet flow field solvers. It is noted that the accuracy of the ice shape predictions is not significantly impacted. A fair balance between accuracy and cost is sought. To accomplish this, three different surface grid densities are considered for this study.

The heat transfer coefficient during the final step involving ice formation is obtained from the skin friction coefficient derived from the airflow field computation. To accurately capture the skin friction coefficient, a properly refined boundary layer zone is essential. An initial $y^+$ estimate of 1.0 is used based on standard mesh generation practices. To accurately capture the laminar sublayer, a $y^+$ value of less than 5.0 is chosen to allow for sufficient grid points within the sublayer. Since, the coefficient of skin friction is a crucial parameter for modeling ice accretion, a $y^+$ value of 1.0 is chosen to ensure accuracy. As mentioned previously, the turbulence model chosen is the k-omega SST which requires a smaller $y^+$ for the proper implementation of its near-wall treatment.

A grid spacing calculator by Pointwise [29] is used to calculate the first cell height corresponding to a $y^+$ value of 1.0. The total number of layers within the boundary layer is set to 30 and the growth rate for the cell height within the boundary layer is set to 1.2 leading to consistent boundary layer mesh refinement for grids considered. A summary of grid specifications is presented in Table 2.

Table 2. Properties corresponding to the different grids considered. [18]

| Property | Mesh 1 | Mesh 2 | Mesh 3 | Mesh 4 |
|---|---|---|---|---|
| **Points on Airfoil** | 100 | 200 | 400 | 400 |
| **Cells on Surface** | 1,980 | 3,980 | 7,980 | 7,980 |
| **Volume Cells** | 2.196e5 | 4.138e5 | 7.929e5 | 5.555e5 |
| **Layers within BL** | 30 | 30 | 30 | 20 |
| **Growth Rate within BL** | 1.2 | 1.2 | 1.2 | 1.2 |
| **Initial $y^+$** | 1 | 1 | 1 | 3 |
| **First Cell Height** | 3.765e-6 m | 3.765e-6 m | 3.765e-6 m | 11.29e-6 m |

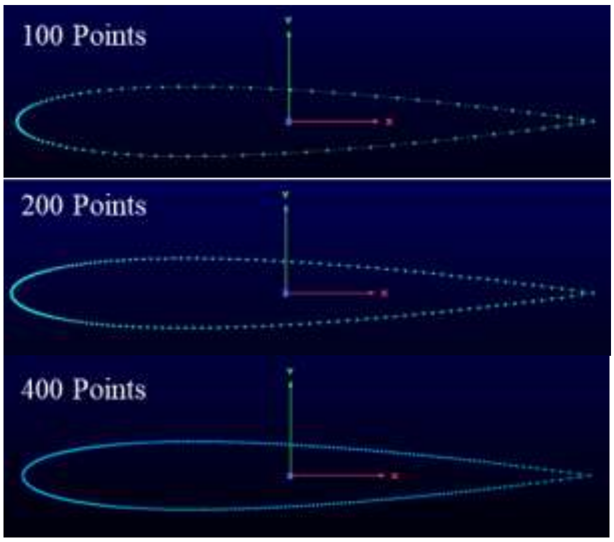

Fig. 3: Illustration for surface grid refinement

The three surface point distributions of 100, 200, and 400 surface points along the surface are illustrated in Fig. 3. The refinement in the leading edge region for each of the three surface density grids is represented in Fig. 4. It may be observed that the point spacing near the leading edge is reduced, leading to tighter clustering, for each of the three grids to locally increase the density of points at the leading edge. Since most of the accreted ice deposits near the leading edge and the strongest flow field gradients occur in this region, it is important for this to be sufficiently refined.

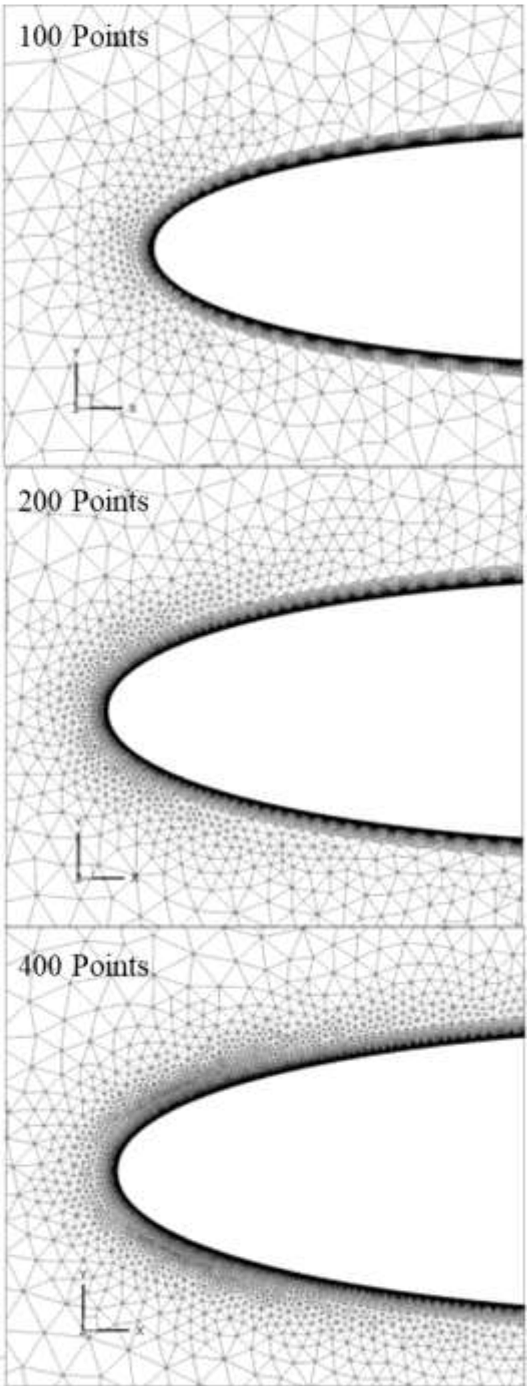


Fig. 4: Airfoil leading edge mesh resolution

ANSYS Fluent models and set-up are consistent across all the grids. The values of the pressure coefficient and the skin friction coefficient corresponding to the three surface grid densities are shown in Fig. 5. It may be observed that while there are not many discernible differences in the pressure coefficient values, the skin friction coefficient values differ, especially in regions away from the leading edge with the 100-point surface grid density mesh predicting the smallest values of skin friction and the 400 point surface grid density mesh predicting the largest values of skin friction. Larger values of the skin friction coefficient will result in higher heat transfer which will lead to thicker ice.

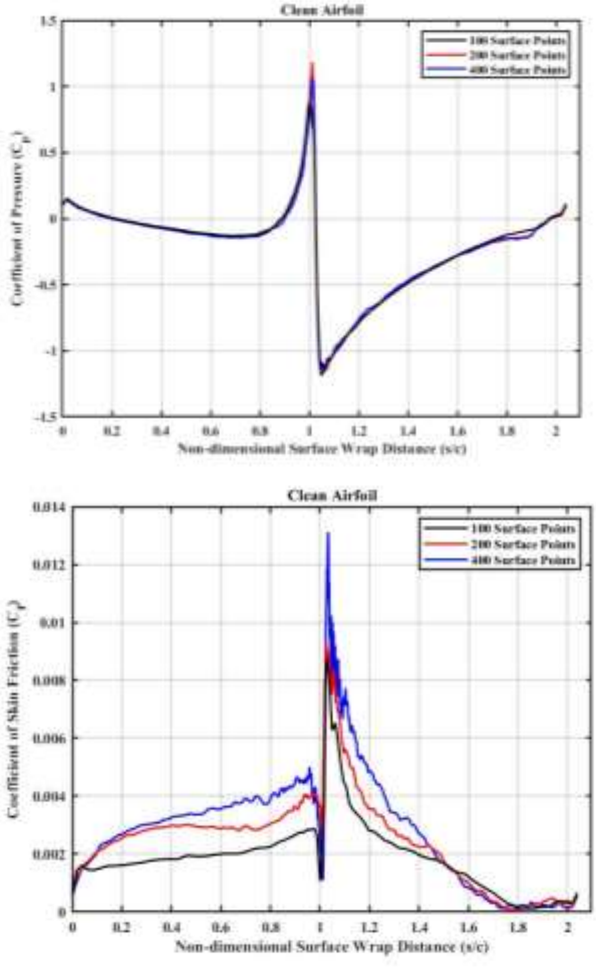


Fig. 5: Effect of grid resolution on the pressure coefficient and the skin friction

The only noticeable difference in the pressure coefficient values is that the 100-point surface density mesh predicts a smaller value for the pressure coefficient at the stagnation point. The exact location of the stagnation point may be incorrectly determined by this particular mesh because of the relatively large spacing between subsequent grid points. The spatial marching process along the surface is initialized at the stagnation point within the ice accretion module. Incorrect prediction of the location of the stagnation point may impact the location of the maximum thickness of the predicted ice shape. All three surface density grids predict the same location for the suction peak and the corresponding values of the pressure coefficient are also the same.

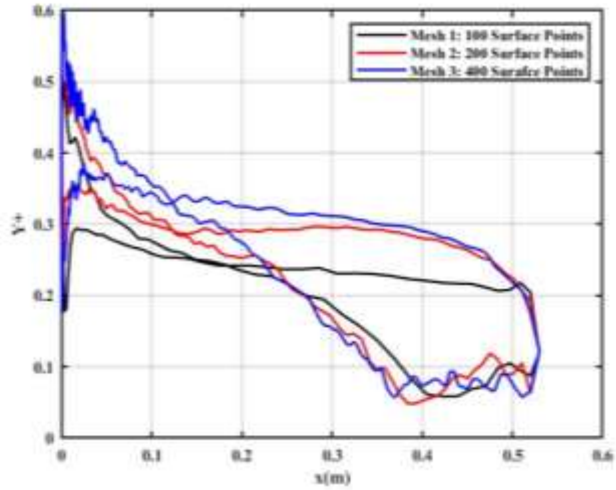


Fig. 6: Effect of grid resolution on wall $y^+$ values

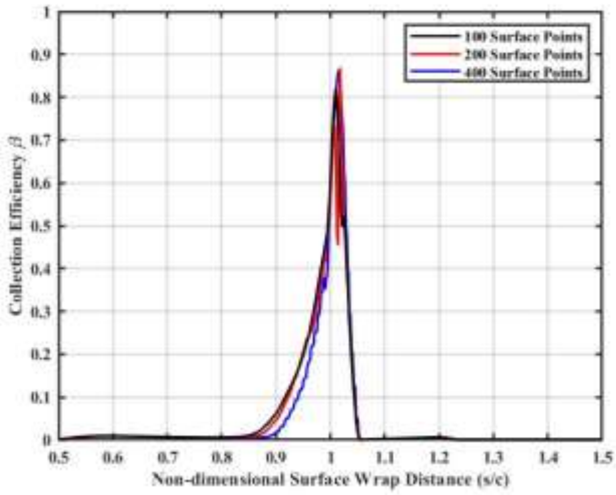


Fig. 7: Effect of grid resolution on collection efficiency values

The actual $y^+$ values obtained from the airflow field simulations from ANSYS Fluent have been shown in Fig. 6. Although the initial first cell height was calculated based on an assumption of $y^+$ equal to 1.0, it is seen that the largest value of $y^+$ is 0.6 resulting in a finer grid than was initially expected. This resolution is fine enough to capture the skin friction effects sufficiently for the final step of ice accretion.

From the droplet phase solver, GTDROP-Uns, the collection efficiency as a function of the non-dimensional surface wrap distance, starting at the trailing edge and proceeding in the clockwise direction is plotted in Fig. 7. The wetted region observed in Fig. 7 represents a dissymmetry with a larger area of the lower surface of the airfoil, close to the leading edge, observing non-zero collection efficiency values. This is because of the positive angle of attack of 3.5°. Numerical oscillations are observed for the 400-point surface density grid between s/c values of 0.9 and 1.0. This could be because the tighter spacing leads to uneven or skewed cell aspect ratios in this region since the first cell height and boundary layer growth rate are consistent across the three grids considered.

### 3.1 Ice Accretion: Single-Step Approach

The results presented under this section are for a single-step icing computation over 231 seconds. The pressure coefficient, skin friction coefficient, surface temperature, and droplet impingement collection efficiency are obtained only once on a clean surface.

The ice shape predictions for the three different surface point densities are shown in Fig. 8. It may be observed that the extent of the wetted region and ice accretion is accurately captured by all three grids on both the upper and the lower airfoil surfaces. The thickness of the ice accreted is overpredicted on the upper surface and under-predicted on the lower surface. The stagnation point ice thickness is similarly predicted by all three meshes. A well-formed ice horn is present on the upper surface of the 400-point surface density grid ice shape prediction. While this is slightly captured by the 200-point surface density grid, the 100-point surface density grid completely misses it. The angle of this ice horn matches the experimental ice shape; however, the location and length are off. The lower ice horn is uncaptured by all the grids. The numerical oscillations observed for the 400-point surface density grid under Fig. 7 are manifested as irregularities in the ice shape predicted by the 400-point surface density grid on the lower surface of the airfoil. The thickness here is also slightly under-predicted compared to the two other grids which may also be attributed to the collection efficiency values observed on the lower surface.

From Fig. 8 it may be deduced that the 400 point surface density grid is the only one which managed to capture the upper ice horn indicating that a finer spatial discretization did lead to an improvement in the ice shape prediction. However, the 400-point surface density grid is computationally costly and time-consuming. To reduce the computational cost yet retain the surface point density, the total number of volume cells for the mesh must be reduced. For "Mesh 4" listed under Table 2 this is accomplished by coarsening the boundary layer and increasing the first cell height such that the initial guess value for $y^+$ is equal to 3.0 instead of 1.0. A viscous sublayer for turbulent low is up to a $y^+$ value of 5.0. Therefore, an initial first cell height corresponding to $y^+$ equal to 3.0 still allows for the viscous sublayer to be sufficiently modeled to accurately capture the near-wall turbulence effects.

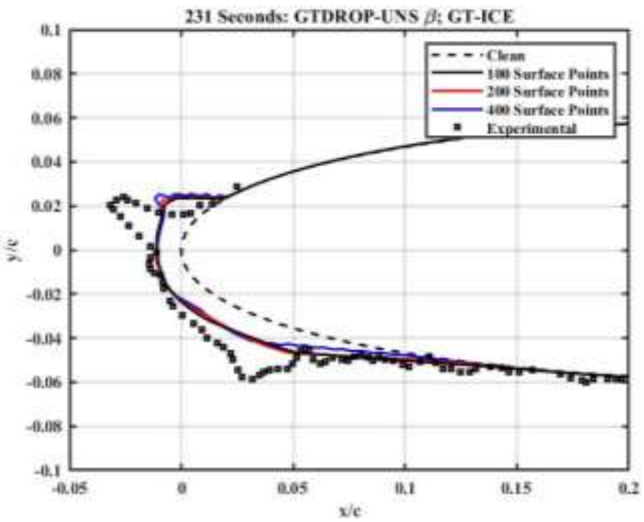


Fig. 8: Effect of grid resolution on predicted ice shapes

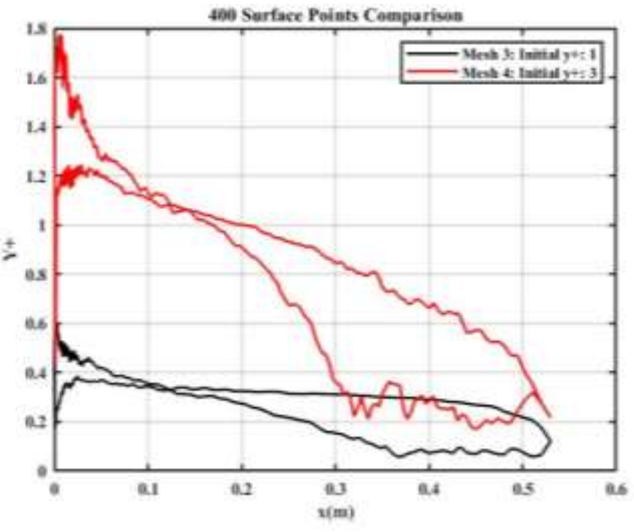


Fig. 9: Effect of boundary layer resolution on wall $y^+$ values

Fig. 9 shows the actual values of $y^+$ observed for the two 400-point surface density meshes. While it is observed that the largest $y^+$ observed for mesh 3 is 0.6, as has been noted earlier, the largest $y^+$ observed for mesh 4 with the boundary layer coarsening is 1.8. This is still sufficiently fine to capture near-wall turbulence effects. An increase in the first cell height led to an approximately 30% reduction in the total volume of cells from around 793,000 to 555,500.

To ascertain the impact of coarsening the boundary layer on the skin friction coefficient values obtained on the two grids, the results are plotted in Fig. 10. Both grids result in very similar predictions close to the leading edge, which is a region of vital importance for ice accretion computations. Mesh 4 predicts slightly larger values of the skin friction coefficient on the lower surface close to the leading edge. Although, this region is of significance for ice accretion, these differences are not expected to result in vastly different ice shape predictions.

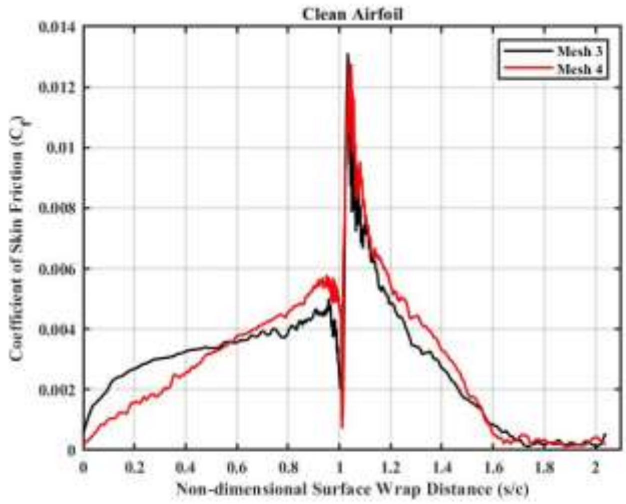


Fig. 10: Skin friction coefficient obtained using the 400-point surface density grids, 3 (refined BL region) and 4 (coarsened BL region).

The ice shape predictions for the two 400-point surface density grids are plotted in Fig. 11. Not many differences are noticed, except that the upper ice horn is better developed for mesh 3 and that the ice shape predicted by mesh 4 is thicker on the lower surface. This is in closer agreement with the ice thickness predictions of meshes 1 (100 point) and 2 (200 point) from Fig. 8 and could be because of better aspect ratios due to an increase in the first cell height for mesh 4. Overall, the thickness and extent of ice accretion predicted by both meshes are similar.

The increase in the first cell height and the subsequent coarsening of the boundary layer do not impact the ice shape prediction greatly, although they do considerably lower the computational cost. Exploiting this advantage, mesh 4 is used for the multi-step studies in place of mesh 3 for the 400-point surface density grid.

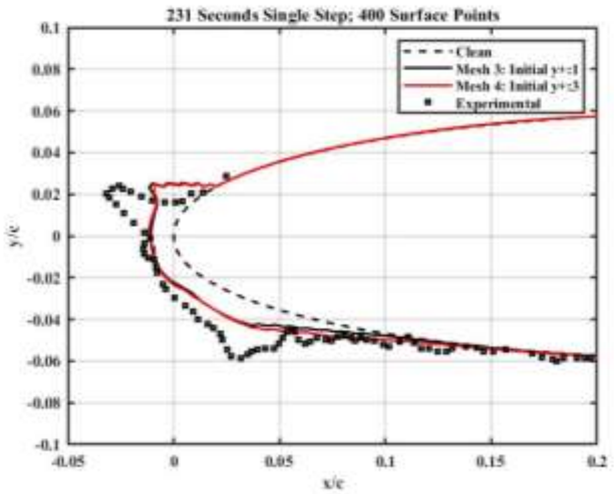


Fig. 11: Effect of boundary layer resolution on ice shape predictions

## 3.2 Ice Accretion: Multi-Step Approach

As explained in detail under the methodology section, for the multi-step simulations, the air and droplet flow fields are recomputed after regular time intervals such that the relevant flow parameters such as the pressure coefficient, skin friction coefficient, surface temperature, and the droplet collection efficiency are updated to reflect the changes in the airframe geometry due to the formation of ice. Similar to the grid density arguments, the time step chosen is dependent on the accuracy of the comparison between the final predicted ice shape and the experimentally observed ice shape and the computational cost associated with re-meshing and re-computing the flow fields. From prior structured grid case studies [18], [19], [22], [30], a time step of 60 to 90 seconds is deemed adequate for the re-computation of the air and droplet flow fields.

Such a large time step is facilitated by the argument that the difference in time scales between the aerodynamic changes in the flow field and the ice accretion is large enough to accommodate a loosely coupled process. The total ice accretion time is divided into three steps for this study, with each time step equal to 77 seconds. Three different surface density grids are considered, meshes 1, 2, and 4.

The ice shape predictions at the end of each time step are shown in Fig. 12. The experimental ice shape is represented using black squares. It can be observed that the three surface density grids are consistent in their predictions for the thickness and extent of ice accretion. The 100-point surface density grid predicts the most deposition and the smoothest ice shape at the end of 231 seconds. Some of the jaggedness of the experimental ice shape is captured by the 200-point surface density grid close to the leading edge. Artificial oscillations are observed on the lower surface of the 400 point surface density grid. The location of the upper ice horn is being captured by the tools in some capacity; however, the extent is not being accurately predicted. None of the grids manage to predict the lower ice horn even for a multi-step simulation.

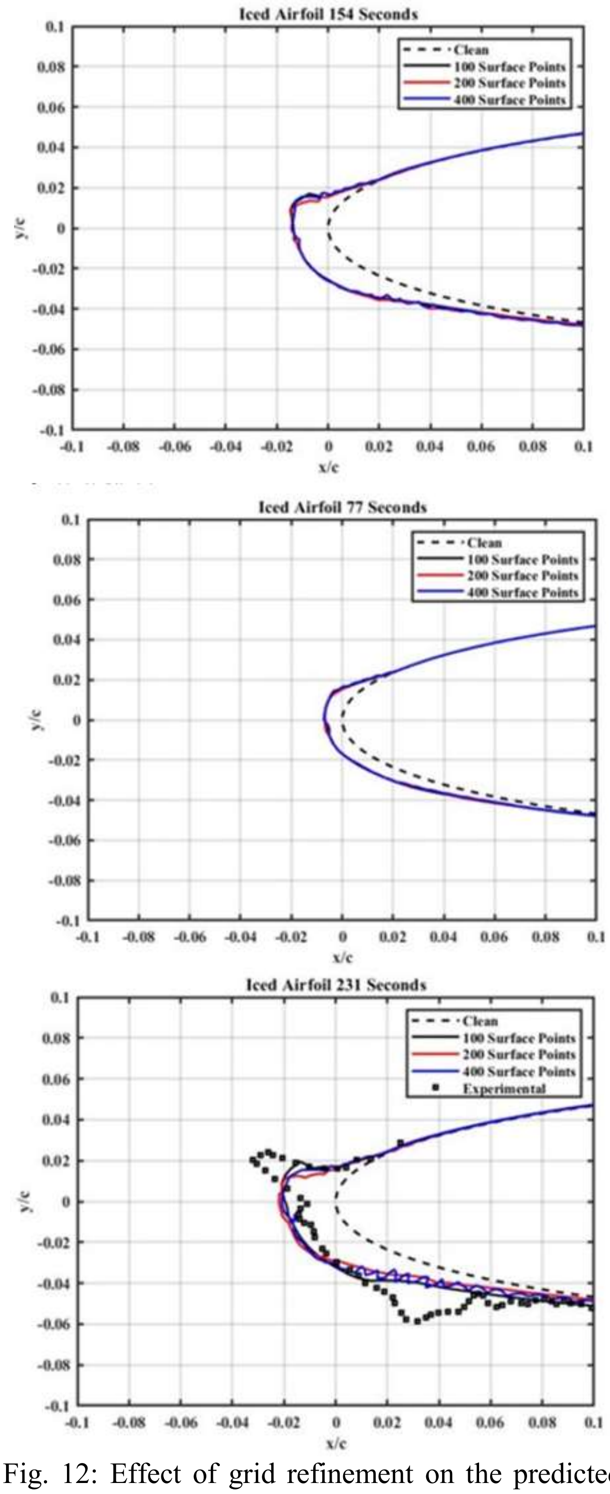


Fig. 12: Effect of grid refinement on the predicted ice shapes multi-step ice accretion

The computational time required is directly proportional to the number of streamwise points. From Fig. 8, although the 400-point surface density grid captures the upper ice horn better, the computational requirement for this grid is twice as much. The changes in the ice shape predictions between the 200 and the 400-point surface grids are negligible with the 400-point grid performing marginally better. Considering the comparison with experimental data for the predictions obtained using each grid as well as the associated computational cost of the entire simulation, the 200 surface point grid is established as a fair balance.

## 4 Conclusion and Recommendations

Grid sensitivity studies are performed for the NACA0012 glaze ice case using a combination of in-house and commercially available tools. It is established that the 200-point surface density grid is adequate to determine the ice shape for the case, and it is determined to be an acceptable balance between the accuracy of the final predicted ice shape and the computational cost associated with the entire process. The 400-point surface density grid is computationally very expensive. It also exhibits numerical oscillations in the final step of the multi-step process which are likely a consequence of numerical issues.

While the resolution of the boundary layer does have an impact on the determination of the coefficient of skin friction, heat transfer, and consequently the ice shape, coarsening the $y^+$ at the wall from 1.0 to 3.0 does not have a significant impact on the results, in this case, other than slightly under-predicting the upper ice horn. Although, coarsening the initial $y^+$ guess has a significant impact in terms of the reduction of computational cost, making the use of this grid more viable, particularly for multi-step simulations where the flow field needs to be updated periodically. However, it must be noted that even after the increase in the $y^+$ at the wall to 3.0, it is still smaller than 5.0 to facilitate enough grid points within the laminar sublayer such that the near wall behavior can be accurately captured. For the multi-step process some of the irregularities in the ice shape are better captured compared to a single-step process; however, the ice shape being predicted is thicker close to the leading edge. All grids perform similarly, within reason, for the multi-step ice accretion process.

To further enhance the ice accretion prediction capabilities of the solver considered in this study, it would be beneficial to investigate the impact of laminar to turbulent boundary layer transition. The thicker ice shape close to the stagnation region is because the solver predicts a turbulent boundary layer in this region which leads to a higher heat transfer coefficient. It is possible that this region remains laminar and transition is not accurately captured.

Additionally, the heat transfer coefficient in this work depends on the skin friction coefficient through the Reynolds Analogy. Additional studies involving the validation of the computed heat transfer coefficients against available experimental data would be beneficial. Other models to compute the heat transfer coefficient should also be explored.

A crucial factor in play for the heat transfer calculations is the surface roughness. A change in the surface roughness influences the surface flow field parameters. However, this roughness is orders of magnitude smaller than what can be accurately resolved by CFD grids. Therefore, there is a requirement to explore models that can properly capture the increase in skin friction associated with an increase in surface roughness.

*References:*

[1] Laurendeau, E., Bourgault-Cote, S., Ozcer, I. A., Hann, R., Radenac, E., and Pueyo, A. "Summary from the 1st AIAA ice prediction workshop." *AIAA Aviation 2022 Forum*, Chicago, Illinois, USA, 2022. https://doi.org/10.2514/6.2022-3398.

[2] Laurendeau, E., Blanchet, M., Zayni, M. K., Hann, R., Radenac, E., Mussa, I., and Pueyo, A. "Summary from the 2nd AIAA Ice Prediction Workshop." *AIAA AVIATION FORUM AND ASCEND 2024*, Las Vegas, Nevada, USA, 2024. https://doi.org/10.2514/6.2024-3604.

[3] Baumert, A., Bansmer, S., Trontin, P., and Villedieu, P. "Experimental and numerical investigations on aircraft icing at mixed phase conditions." *International Journal of Heat and Mass Transfer* 123 (2018): 957-978. https://doi.org/10.1016/j.ijheatmasstransfer.2018.02.008.

[4] Radenac, E., Gaible, H., Bézard, H., and Reulet, P. "IGLOO3D computations of the ice accretion on swept-wings of the SUNSET2 database." No. 2019-01-1935, SAE Technical Paper, 2019. https://doi.org/10.4271/2019-01-1935.

[5] Son, C., Oh, S., and Yee, K. "Development of 2nd generation ice accretion analysis program for handling general 3-D geometries." *Journal*

*of computational fluids engineering* 20.2 (2015): 23-36. https://doi.org/10.6112/kscfe.2015.20.2.023.

[6] Gori, G., Zocca, M. A. R. T. A., Garabelli, M., Guardone, A., and Quaranta, G. "PoliMIce: A Simulation Framework for Three-dimensional Ice Accretion." *Applied Mathematics and Computation*, 2015, 96-107. https://doi.org/10.1016/j.amc.2015.05.081.

[7] Gori, G., Bellosta, T., Guardone, A.. *"Numerical Simulation of In-Flight Icing Under Uncertain Conditions,"* in Habashi, W.G. (eds) Handbook of Numerical Simulation of In-Flight Icing. Springer, Cham. https://doi.org/10.1007/978-3-030-64725-4_31-1

[8] Cinquegrana, D., D'Aniello, F., de Rosa, D., Carozza, A., Catalano, P., and Mingione, G. "A CIRA 3D Ice Accretion Code for Multiple Cloud Conditions Simulations." No. 2023-01-1461. *SAE Technical Paper*, 2023. https://doi.org/10.4271/2023-01-1461.

[9] Capizzano, F., and Iuliano, E. "A eulerian method for water droplet impingement by means of an immersed boundary technique." *Journal of Fluids Engineering* 136.4 (2014): 040906. https://doi.org/10.1115/1.4025867.

[10] Bourgault, Y., Ziad B., and Wagdi G. H. "Three-dimensional Eulerian approach to droplet impingement simulation using FENSAP-ICE, Part 1: Model, algorithm, and validation." *Journal of aircraft* 37.1 (2000): 95-103. https://doi.org/10.2514/2.2566.

[11] Ozcer, I. A., Baruzzi, G. S., Reid, T., Habashi, W. G., Fossati, M., and Croce, G. "FENSAP-ICE: Numerical prediction of ice roughness evolution, and its effects on ice shapes." No. 2011-38-0024. *SAE Technical Paper*, 2011. https://doi.org/10.4271/2011-38-0024.

[12] I. Ozcer, G. Moula, J. Page, A. Zanon, M. De Gennaro, R. Llamas, IMPACT: experimental and numerical ice shapes on swept-wing models with straight and undulated leading edges, *2024 AIAA SciTech Forum and Exposition*, https://doi.org/10.2514/6.2024-4160, July 2024.

[13] Mussa, Ifrah & Lin, Yujing & Wang, Jian, "Comparison Criteria for Ice Accretion on an Aerofoil Surface," *Proceedings of the 14th World Congress in Computational Mechanics*, 2020, https://doi.org.10.23967/wccm-eccomas.2020.087.

[14] Szilder, K, and Lozowski, E. P. "Three-dimensional numerical simulation of ice accretion using a discrete morphogenetic approach." *9th AIAA Atmospheric and Space Environments Conference*, Denver, Colorado, USA, 2017. https://doi.org/10.2514/6.2017-3418.

[15] Zayni, M. K., Blanchet, M., and Laurendeau, E. "Recent developments of the multi-physics solver champs-ice." *Proceedings of the Canadian Society for Mechanical Engineering International Congress*, Sherbrooke, QC, Canada, 2023.

[16] Semenova, Irina, and Ichiro Hagiwara. "Explicit Method to Optimize Surface Mesh Quality." *CiteSeerX*.

[17] Hann, Richard, Müller, N. C., Wallisch, J., and Lindner, M. J. *"UAV Icing: Experimental validation data for predicting ice shapes at low Reynolds numbers."* 2023.

[18] Gupta, A., *"Application of Extended Messinger Model for Ice Accretion on Complex Geometries."* Ph.D. Dissertation, Georgia Institute of Technology, 2021, [Online]. http://hdl.handle.net/1853/66084.

[19] Kim, J. W., *"Development of a physics based methodology for the prediction of rotor blade ice formation."* Ph.D. Dissertation, Georgia Institute of Technology, 2015, [Online]. http://hdl.handle.net/1853/54390.

[20] "Density Based Solver," ANSYS Fluent 12.0 Theory Guide, August 2019, [Online]. https://www.afs.enea.it/project/neptunius/docs/fluent/ (Accessed Date: December 15, 2024).

[21] Sutherland, W., "XXXVII. The viscosity of mixed gases," *The London, Edinburgh, and Dublin Philosophical Magazine and Journal of Science*, vol. 40, no. 246, pp. 421-431, 1895. https://doi.org/10.1080/14786449508620789.

[22] Gupta, A, Sankar, L., and Kreeger, R., "Effect of Time-Step Duration and Other Parameters on Ice Accretion." *AIAA AVIATION 2022 Forum*, Chicago, Illinois, USA, 2022. https://doi.org/10.2514/6.2022-3397.

[23] Thwaites, B., "Approximate calculation of the laminar boundary layer," *Aeronautical Quarterly*, vol. 1, no. 3, pp. 245-280. https://doi.org/10.1017/S0001925900000184.

[24] Kays, W. M., *Convective heat and mass transfer*. Tata McGraw-Hill Education, 2011.

[25] Von Doenhoff, A. E. and Horton, E. A., "A low-speed experimental investigation of the effect of a sandpaper type of roughness on boundary-layer transition," No. NACA-TR-1349, 1958, [Online]

https://ntrs.nasa.gov/citations/19930092337 (Accessed Date: December 15, 2024).

[26] Myers, T. G., "Extension to the Messinger model for aircraft icing," *AIAA journal*, vol. 39, no. 2, pp. 211-218, 2001. https://doi.org/10.2514/2.1312.

[27] Hill, J. M., *One-dimensional Stefan problems: an introduction*. Longman Sc & Tech, 1987.

[28] Wright, W. and Rutkowski, A., "Validation Results for LEWICE 2.0," NASA, Nov 1998.

[29] "Compute Grid Spacing for a Given Y+," Pointwise, August 2019. [Online]. https://www.pointwise.com/yplus/index.html (Accessed Date: December 15, 2024).

[30] Gupta, A., Halloran, E., Sankar, L. N., Palacios, J., and Kreeger, R. E.: "Development and Validation of Physics Based Models for Ice Shedding," Proceedings of the 44th European Rotorcraft Forum, 2018, Delft, Netherlands, [Online] https://ntrs.nasa.gov/citations/20180006892 (Accessed Date: December 15, 2024).

**Contribution of Individual Authors to the Creation of a Scientific Article (Ghostwriting Policy)**

Both authors contributed to the work including the problem formulation, tool and methodology development, grid generation, flow-field, droplet impingement and ice accretion simulations, the post-processing and interpretation of results, and the compilation of this paper.

**Sources of Funding for Research Presented in a Scientific Article or Scientific Article Itself**

Partially funded by the U.S. Government, the U.S. Army Technology Development Directorate, CCDC AvMC, under Technology Investment Agreement W911W6-17-2-0002, entitled Georgia Tech Vertical Lift Research Center of Excellence (GT-VLRCOE) with Dr. Mahendra Bhagwat as the Program Manager.

**Conflict of Interest**

The authors have no conflicts of interest to declare.